

1
2
3
4
5
6
7
8
9
10
11
12
13
14
15
16
17

REVISION 1

Elastic anomalies across the $P2_1mn \rightarrow Pnm$ structural phase transition in δ -(Al,Fe)OOH

Niccolò Satta^{1,2,3,*}, Giacomo Criniti^{1,†}, Alexander Kurnosov¹, Tiziana Boffa Ballaran¹, Takayuki Ishii⁴ and Hauke Marquardt²

¹Bayerisches Geoinstitut, University of Bayreuth, 95447 Bayreuth, Germany

²Department of Earth Sciences, University of Oxford, OX1 3AN Oxford, United Kingdom

³Institut für Mineralogie, Westfälische Wilhelms-Universität Münster, 48149 Münster, Germany

⁴Institute for Planetary Materials, Okayama University, Misasa, 682-0193 Tottori, Japan

[†]Present address: Earth and Planets Laboratory, Carnegie Institution for Science, 20015 Washington, DC, USA

*Corresponding author: Niccolò Satta (nsatta@uni-muenster.de)

18

Abstract

19

20

21

22

23

24

25

26

27

28

29

30

31

32

33

34

35

36

Hydrogen may be recycled into the Earth's lower mantle by subduction and stabilized in solid solutions between phase H (MgSiO_4H_2), δ - AlOOH , ϵ - FeOOH , and SiO_2 post-stishovite. In high-pressure oxyhydroxide phases, hydrogen is incorporated following the typical (OHO) sequence, adopting the asymmetric configuration $\text{O-H}\cdots\text{O}$ that evolves into a symmetric disordered state upon compression. Moreover these iron-/aluminum-bearing oxyhydroxides [δ -(Al,Fe)OOH] present a structural phase transition from $P2_1nm$ to $Pnmm$ as pressure increases. Here, the single-crystal elasticity of the $P2_1nm$ phase of δ -($\text{Al}_{0.97}\text{Fe}_{0.03}$)OOH has been experimentally measured across the $P2_1nm \rightarrow Pnmm$ transition up to 7.94(2) GPa by simultaneous single-crystal X-ray diffraction (XRD) and Brillouin spectroscopy at high pressures. The transition appears to be continuous, and it can be described with a second, fourth and six order terms Landau potential. Our results reveal an enhanced unit-cell volume compressibility, which is linked to an increase of the b - and a -axes linear compressibility in the $P2_1nm$ phase of δ -($\text{Al}_{0.97}\text{Fe}_{0.03}$)OOH prior to the transition. In addition, we observed the presence of elastic softening in the $P2_1nm$ phase that mostly impacts the elastic stiffness coefficients c_{12} , c_{22} and c_{23} . The observed elastic anomalies cause a significant change in the pressure dependence of the adiabatic bulk modulus (K_S). These results provide a better understanding of the relation between elasticity, $P2_1nm \rightarrow Pnmm$ structural phase transition and hydrogen dynamics in δ -($\text{Al}_{0.97}\text{Fe}_{0.03}$)OOH, which may be applied to other O-H \cdots O-bearing materials.

37

1. Introduction

38

39

40

Hydrogen can be stored in mantle minerals, affecting their physical properties. Investigating its distribution throughout the Earth's interior is thus relevant to understanding deep geodynamic processes and geochemical cycles (Bercovici & Karato, 2003; Ohtani et al., 2004;

41 Ohtani, 2020). In the Earth's interior, hydrogen is mostly present as hydroxyl groups (OH⁻) bonded
42 to the crystal structure of hydrous phases, as well as incorporated as hydrous defect in nominally
43 anhydrous minerals (Ishii et al., 2022; Jacobsen, 2006; Ohtani, 2015).

44 Solid solutions between isostructural compounds phase H (MgSiO₄H₂), δ-AlOOH, ε-
45 FeOOH, and SiO₂ post-stishovite may act as main carriers of hydrogen into the lower mantle due
46 to their ability to remain stable at relatively high-temperatures and pressures (Ishii et al., 2022;
47 Nishi et al., 2019; Ohira et al., 2014). In iron-bearing aluminum oxyhydroxides [δ-(Al,Fe)OOH],
48 hydrogen is expected to be bonded via hydrogen bonds adopting an asymmetrical configuration
49 (O-H···O) at low pressures (Sano-Furukawa et al., 2018). Upon compression, symmetrization of
50 the hydrogen bonds (O-H-O) is achieved with a symmetric proton disordered state acting as a
51 precursor to the symmetrization (Sano-Furukawa et al., 2018). The phenomenon of hydrogen bond
52 symmetrization is predicted to impact physical properties, potentially enhancing the stability of
53 these oxyhydroxides down to the core-mantle boundary (Nishi et al., 2019; Ohira et al., 2014).

54 At ambient conditions, the crystal structure of δ-AlOOH and ε-FeOOH (Supplementary
55 Figure S1a) has space group *P2₁nm* and consists of chains of edge sharing (Al,Fe)O₆ octahedra
56 extending parallel to the **c**-axis and connected with each other through vertices (Bolotina et al.,
57 2008; Komatsu et al., 2006; Kuribayashi et al., 2014; Pernet et al., 1975; Suzuki et al., 2000;
58 Suzuki, 2010). The octahedral cation site is coordinated by three oxygen atoms and three
59 hydroxide, which gives rise to a 2D hydrogen bond network in the **a-b** plane, with the hydrogen
60 bonds lying almost parallel to the [120] direction (Kuribayashi et al., 2014; Sano-Furukawa et al.,
61 2018). Below 10 GPa, a structural phase transition occurs in δ-AlOOH, resulting in the symmetry
62 increasing from *P2₁nm* to *Pnmm* (Supplementary Figure S1b) (Kuribayashi et al., 2014; Sano-
63 Furukawa et al., 2009; Simonova et al., 2020). Within the same pressure range, neutron diffraction

64 experiments by Sano-Furukawa et al. (2018) showed a change in the hydrogen bond from an
65 asymmetric ordered configuration (O-H \cdots O) to a symmetric disordered one where hydrogen
66 atoms are equally distributed between two symmetrically-equivalent sites across the center of the
67 O \cdots O line (Supplementary Figure S1b). The disordering of hydrogen in the 9-18 GPa range has
68 been initially attributed to the presence of proton tunneling, similarly to previous observations in
69 high-pressure H₂O ices (Lin et al., 2011; Meier et al., 2018; Trybel et al., 2020), whereas more
70 recent studies suggested that it is actually dynamic disorder (Meier et al., 2022; Trybel et al., 2021).
71 Centering of the hydrogen bond, i.e. with the hydrogen locked in the mean position along the
72 O \cdots O line and covalently bonded to the two oxygens (O-H-O), occurs in δ -AlOOH at around 16-
73 18 GPa (Sano-Furukawa et al., 2018), or possibly at even lower pressures (14.7 GPa, Trybel et al.,
74 2021). Therefore, proton disordering appears to act as precursor to the hydrogen bond symmetric
75 centered configuration.

76 Theoretical studies suggest that the completion of the symmetrization of the hydrogen
77 bonds would severely alter the elastic properties of δ -AlOOH (Cortona, 2017; Panero & Stixrude,
78 2004; Pillai et al., 2018; Tsuchiya et al., 2002; Tsuchiya & Tsuchiya, 2009). Experimental
79 observations of this occurrence were provided by Brillouin scattering measurements on
80 polycrystalline samples of δ -AlOOH (Mashino et al., 2016) and δ -(Al_{0.95}Fe_{0.05})OOH (Su et al.,
81 2020) that detected a sharp change in acoustic wave velocities at \sim 15 and \sim 20 GPa, respectively.
82 However, previous P - V experimental investigations on δ -(Al,Fe)OOH contrast with this
83 interpretation since a reduction in the axial compressibility was observed at much lower pressures
84 (\sim 8 GPa; e.g., Ohira et al., 2019; Sano-Furukawa et al., 2009), hence suggesting that it is the
85 $P2_1nm \rightarrow Pnmm$ transition that mostly impacts the compression behavior of these oxyhydroxides.

86 At the Fe-rich end of the solid solution series, recent experimental studies pinpointed the
87 $P2_1nm \rightarrow Pnnm$ transition in δ -(Al_{0.3}Fe_{0.7})OOH and ϵ -FeOOH at ~10 GPa and 18 GPa, respectively
88 (Ikeda et al., 2019; Meier et al., 2021; Thompson et al., 2017, 2020). Additionally, a high-to-low
89 spin transition in Fe has been found to occur in ϵ -FeOOH at about 45 GPa (Gleason et al., 2013;
90 Thompson et al., 2020), but the symmetrization pressure in ϵ -FeOOH is still poorly constrained.
91 This has been first suggested to occur around 45 GPa, and linked to the Fe spin transition (Gleason
92 et al., 2013; Xu et al., 2013). However, more recent experimental studies on δ -(Al_{0.3}Fe_{0.7})OOH
93 showed that these are two distinct phenomena (Meier et al., 2022). Other studies suggest the
94 symmetrization to occur at lower pressures, between 10 and 20 GPa, and possibly triggering the
95 $P2_1nm \rightarrow Pnnm$ transition in ϵ -FeOOH (Thompson et al., 2017).

96 Therefore, in spite of the number of recent studies (e.g., Buchen et al., 2021; Insixiengmay
97 & Stixrude, 2023; Luo et al., 2022; Mashino et al., 2016; Meier et al., 2022; Sano-Furukawa et al.,
98 2018; Satta et al., 2021; Strozewski et al., 2023; Thompson et al., 2020; Trybel et al., 2021;
99 Tsuchiya et al., 2020), the relation between elastic behavior, hydrogen bond
100 disorder/symmetrization, and structural phase transition in δ -(Al,Fe)OOH is still poorly
101 constrained, hampering our understanding of the deep recycling of hydrogen into the Earth's lower
102 mantle.

103 Here, we performed simultaneous high-pressure X-ray diffraction (XRD) and Brillouin
104 spectroscopy experiments on δ -(Al_{0.97}Fe_{0.03})OOH samples to provide the first full and
105 comprehensive description of the single-crystal elasticity of the $P2_1nm$ phase of δ -(Al,Fe)OOH at
106 high pressure. Our experiments were performed up to 7.94(2) GPa with relatively small pressure
107 steps across the $P2_1nm \rightarrow Pnnm$ transition in order to better constrain any small elastic change
108 associated with the transition. Our results, that include the description of all the elastic stiffness

109 coefficients at high pressures, provide new insights on the relation between single-crystal elasticity
110 at high pressures, structural transition and proton disordering in $\delta\text{-(Al}_{0.97}\text{Fe}_{0.03}\text{)OOH}$.

111 **2. Materials and Methods**

112 **2.1. Samples**

113 In this study, the same two single-crystal platelets of $\delta\text{-(Al}_{0.97}\text{Fe}_{0.03}\text{)OOH}$ studied at
114 pressures above 8 GPa by Satta et al. (2021), namely H4765x1 and H4765x2, were measured.
115 Details on the synthesis procedure, chemical compositions of each crystal platelet, as well as
116 sample selection, orientation and preparation, can be found in Satta et al. (2021).

117

118 **2.2. High-Pressure Experiments**

119 High-pressure experiments were performed using a BX90 diamond anvil cell (DAC)
120 (Kantor et al., 2012) equipped with Boehler-Almax type diamonds (Boehler & De Hantsetters,
121 2004) having a culet size of 400 μm . A circular pressure chamber (250 μm diameter) was obtained
122 by laser drilling a Re gasket previously indented to a final thickness of about 50 μm . Both sample
123 platelets were loaded in the pressure chamber (Schulze et al., 2017), together with a ruby
124 ($\text{Cr:Al}_2\text{O}_3$) sphere for pressure determination. Ruby fluorescence measurements on the pressurized
125 ruby and on a ruby sphere kept at room pressure were performed before and after each set of
126 experiments. Room pressure and pressurized rubies were kept at the same temperature for at least
127 4 hours before the fluorescence measurements. The ruby calibration of Dewaele et al. (2004) was
128 used to derive pressures from the ruby fluorescence signal.

129 High-pressure experiments were performed in two distinct runs, with He or Ne acting as
130 pressure-transmitting media (Supplementary Table S1). Both Ne and He ensure a quasi-hydrostatic

131 environment within the investigated pressure range (Klotz et al., 2009). Gas loadings were
132 performed using the system installed at the BGI (Kurnosov et al., 2008). Simultaneous single-
133 crystal XRD and Brillouin spectroscopy experiments at high pressure were conducted up to 7.94(2)
134 GPa using the combined XRD and Brillouin spectroscopy system installed at the BGI (Trots et al.,
135 2011, 2013).

136 The unit-cell parameters and volumes of the two single-crystal platelets (Table S1) were
137 determined for each platelet by centering a minimum of 12, and up to 17 Bragg reflections ($21^\circ <$
138 $2\theta < 40^\circ$) belonging to the $\langle 111 \rangle$, $\langle 120 \rangle$, $\langle 021 \rangle$, $\langle 211 \rangle$, $\langle 121 \rangle$, $\langle 030 \rangle$, $\langle 301 \rangle$, $\langle 112 \rangle$, $\langle 031 \rangle$,
139 $\langle 131 \rangle$, $\langle 202 \rangle$, $\langle 212 \rangle$, $\langle 411 \rangle$ and $\langle 222 \rangle$ families of crystallographic planes. The centering routine
140 employed in our study relies on the eight position protocol described by King & Finger (1979) to
141 correct for diffractometer aberrations and sample offsets using a Huber four-circle diffractometer.
142 The diffractometer is equipped with an ultra-high intensity $\text{MoK}\alpha$ rotating anode X-ray source
143 (FR-E+ SuperBright, Rigaku) coupled with multilayer VaryMax™ focusing optics and a point
144 detector, and is operated using the SINGLE software (Angel & Finger, 2011). Due to the non-
145 homogeneous $K\alpha_1/K\alpha_2$ ratio produced by the X-ray focusing optics, individual reflection profiles
146 were refitted using the WinIntegrStp software (Angel, 2003). The unit-cell parameters of the two
147 crystals (Table S1) are not identical due to their slightly different Fe contents, that is 3.24(15) wt%
148 for H4765x1 and 2.71(15) wt% for H4765x2 (Satta et al. 2021). Note, however, that such subtle
149 difference in Fe content has a negligible effect on both the compressibility and elasticity behavior
150 of the two crystals (see Results and Discussion below).

151 Brillouin spectroscopy experiments were performed in a 80° forward symmetric scattering
152 geometry (Speziale et al., 2014; Whitfield et al., 1976) using a coherent Verdi V2 solid state
153 Nd:YVO₄ frequency doubled laser ($\lambda_0 = 532.0$ nm), and a six-pass scanning Fabry-Pérot

154 interferometer (Lindsay et al., 1981; Sandercock, 1982) coupled to a single pixel photon counter
155 detector. Measurements were performed at a total of nine distinct pressure points, from room
156 pressure to 7.94(2) GPa. Brillouin spectra were collected for each pressure point and for each
157 platelet at different rotation angles (χ) with 10-20° interval over a 360° angular range. The external
158 scattering angle (θ_{ext}) was calibrated with a reference silica glass. Frequency shifts were
159 converted into velocities using the equation (Speziale et al., 2014; Whitfield et al., 1976):

$$160 \quad v = \frac{\Delta\omega \lambda_0}{2 \sin\left(\frac{\theta_{ext}}{2}\right)} \quad (1)$$

161 Where $\Delta\omega$ is the measured frequency shift, λ_0 is the laser wavelength in air (and vacuum) and
162 $\theta_{ext} = 80^\circ$. The $P2_1nm$ phase of δ -(Al,Fe)OOH crystalizes in the orthorhombic system, hence its
163 single-crystal elasticity is described by nine independent, non-zero elastic stiffness coefficients
164 (c_{ij}). In Voigt notation (Nye, 1985), these are: c_{11} , c_{22} , c_{33} , c_{44} , c_{55} , c_{66} , c_{12} , c_{13} , c_{23} . All nine c_{ij} were
165 constrained at each pressure point (Table S3) through a least-square fit of the Christoffel equation
166 (Haussühl, 2007):

$$167 \quad |c_{ijkl}n_jn_l - \rho v^2 \delta_{ik}| = 0 \quad (2)$$

168 where c_{ijkl} are the elastic stiffness coefficients in full tensorial notation, n_j and n_l are the phonon
169 direction cosines, ρ is the density and δ_{ik} is the Kronecker delta. The least-square fitting routine of
170 the Christoffel equation was implemented in an Origin software (OriginLab corporation,
171 Northampton, MA, USA) script following the formulation by Buchen (2018). The densities of the
172 two platelets were calculated taking into account the different compositions of the two crystals
173 (Table S1) as well as the fact that the synthesis was performed using a 96% ^{57}Fe enriched starting
174 material (Satta et al. 2021). The two densities were found to be identical within uncertainties, hence
175 an averaged value (Table S3) was used in the fitting routine. Voigt and Reuss bounds of the

176 adiabatic bulk (K_s) and shear moduli (G) were calculated at each pressure point using the c_{ij} and
177 the elastic compliance coefficients, s_{ij} , respectively (Table S4).

178 3. Results and Discussion

179 3.1. $P2_1nm \rightarrow Pnmm$ transition pressure

180 The evolution of the $0\bar{3}0$ reflection of sample H4765x2 was followed as a function of
181 pressure in order to pinpoint the $P2_1nm \rightarrow Pnmm$ transition pressure (Figure 1). This reflection is
182 intense in the $P2_1nm$ space group and is a systematic extinction in the $Pnmm$ space group in which
183 only the $0k0$, with $k=2n$ reflections can be observed. The intensity of the $0\bar{3}0$ reflection has been
184 normalised with respect to that of the $1\bar{3}0$ reflection, which is present in both $P2_1nm$ and $Pnmm$
185 space groups. For this purpose, the omega rocking curves (inset in Figure 1) for the two reflections
186 were measured at each pressure using omega steps of 0.005° and exposure times up to 10 s/step.
187 The crystalline quality of both platelets, assessed from the full width half maximum of investigated
188 reflection peaks in omega rocking curves, was found to be preserved after the phase transition. Our
189 results show that the intensity ratio $I(0\bar{3}0)/I(1\bar{3}0)$ decreases continuously and non-linearly with
190 pressure, eventually reaching zero with the disappearance of the $0\bar{3}0$ reflection between P_{ruby}
191 7.59(3) GPa and 7.94(2) GPa. If we assume that this intensity ratio varies as the square of the order
192 parameter, Q , driving the $P2_1nm \rightarrow Pnmm$ phase transition, then a Landau free energy (G) expansion
193 having second, fourth and sixth order terms $G = \frac{1}{2}a(P - P_c)Q^2 + \frac{1}{4}bQ^4 + \frac{1}{6}cQ^6$ (e.g., Carpenter
194 et al., 1998) can be used to derive the variation of Q^2 with pressure (Boffa Ballaran et al., 2000;
195 Carpenter et al., 1990):

$$196 \quad Q^2 = \frac{I(0\bar{3}0)}{I(1\bar{3}0)} = \frac{1 - \frac{b}{a} + \sqrt{\left(\frac{b}{a}\right)^2 - 4\frac{c}{a}(P - P_c)}}{\frac{c}{a}} \quad (3)$$

197 With P_c being the transition pressure, and a , b and c the Landau coefficients. Note that only relative
198 values of the coefficients have been used since the absolute values of a , b and c cannot be
199 constrained without additional information (e.g. excess heat capacity). Fit to the intensity ratio data
200 (Figure 1) gives $P_c = 7.7(2)$ GPa, and the ratio between the coefficients (in GPa) are 10(5) and
201 56(19) for b/a and c/a , respectively.

202 The disappearance of the 010 and 120 reflections of the δ -AlOOH end-member has been
203 previously observed to occur at lower pressures (i.e. at 4.83 GPa and at 6.53 GPa, respectively) in
204 neutron diffraction experiments (Sano-Furukawa et al., 2009). On the other hand, single-crystal
205 X-ray diffraction experiments on the same end-member δ -AlOOH, reported the disappearance of
206 selected $0kl$ reflections with $k + l = \text{odd}$ (i.e. systematic extinction in the $Pnmm$ space group)
207 between 6.1 and 8.2 GPa (Kuribayashi et al., 2014), hence in excellent agreement with our results.
208 The disappearance of the $0\bar{3}0$ reflection is associated with a change in the pressure dependence of
209 the unit-cell axial ratios a/b , b/c and a/c (Supplementary Figure S2), which becomes particularly
210 evident when our data are plotted together with those of the $Pnmm$ phase of δ -(Al_{0.97}Fe_{0.03})OOH
211 from Satta et al. (2021). A similar behavior in axial ratios was previously observed within the same
212 pressure range in δ -AlOOH (Kuribayashi et al., 2014; Sano-Furukawa et al., 2009),
213 (Al_{0.832}Fe_{0.117})OOH_{1.15} and (Al_{0.908}Fe_{0.045})OOH_{1.14} (Ohira et al., 2019), suggesting that the
214 incorporation of about 3% of Fe³⁺ into the δ -AlOOH structure has a negligible effect on the
215 $P_{2_{1nm} \rightarrow Pnmm}$ transition pressure. Note that larger Fe contents, however, are expected to increase
216 the transition pressure, since the $P_{2_{1nm} \rightarrow Pnmm}$ phase transition in the end-member ϵ -FeOOH was
217 observed at 18 GPa (Thompson et al., 2020).

218 Typically, a substituting atom in a solid solution only affects the transition point of the end-
219 member once the microscopic strain fields created by the individual substitutions start to overlap.

220 As Fe^{3+} atoms are added into the $\delta\text{-AlOOH}$ structure, we would expect the $P2_1nm \rightarrow Pnnm$
221 transition pressure to remain constant below a critical composition, which is a direct reflection of
222 the magnitude of the strain fields created by the cation substitution (e.g., Boffa Ballaran et al.,
223 2000; Carpenter et al., 1999; Carpenter et al., 2009; Hayward & Salje, 1996). As there are two
224 cation sites in the unit-cell, the richest Fe-bearing $\delta\text{-AlOOH}$ studied by Ohira et al. (2019) (i.e.,
225 sample Fe12) consist of \sim one atom of Fe^{3+} for every 4 unit-cells. Since no effect on the transition
226 pressure has been observed also for our samples, we expect that a larger concentration of Fe is
227 necessary to observe any change in the behavior of the $P2_1nm \rightarrow Pnnm$ transition as a result of the
228 Al-Fe cation substitution.

229

230 **3.2. Compression behavior**

231 The unit-cell volumes of H4765x1 and H4765x2 are listed in Supplementary Table S1, and
232 their variations with pressure are reported in Figure 2a. The two platelets show the same
233 compressional behavior up to the last pressure point measured. Only unit-cell volumes observed
234 at $P_{\text{ruby}} \leq 6.46(2)$ GPa have been fitted using a 3rd-order Birch-Murnaghan equation of state (BM3)
235 (Birch, 1947) implemented in the EoSFit7 software (Angel et al., 2014) to give insight on possible
236 volume anomalies associated with the $P2_1nm \rightarrow Pnnm$ transition. The volume at room pressure, V_0 ,
237 as well as the isothermal bulk modulus, K_{T0} , and its pressure derivative, K'_{T0} , were fitted using
238 data weighted by the uncertainties in both P and V . The resulting BM3 parameters are reported in
239 Supplementary Table S2.

240 The value of 150.6(11) GPa for K_{T0} obtained in this study is in good agreement with
241 previous experimental studies on the $P2_1nm$ phase of $\delta\text{-AlOOH}$ and $\delta\text{-(Al,Fe)OOH}$ (Ohira et al.,
242 2019; Sano-Furukawa et al., 2009) which, however, have used a 2nd-order Birch-Murnaghan for

243 fitting the P - V data. Our results, instead, tightly constrain the K'_{T0} of the $P2_1nm$ phase of δ -
244 $(Al_{0.97}Fe_{0.03})OOH$, which appears to be slightly smaller than 4 (Supplementary Table S2).
245 Additionally, it is possible to observe a subtle deviation of the volume data from the BM3 EoS fit
246 at $P_{\text{ruby}} > 6.46(2)$ GPa (Figure 2a and inset). Specifically, the observed volumes are smaller than
247 those predicted by the BM3, suggesting a softening of K_T prior to the $P2_1nm \rightarrow Pnmm$ transition.
248 Similar observations have been reported for high-pressure H_2O ices (e.g. Méndez et al., 2021; Shi
249 et al., 2021; Sugimura et al., 2008) and other mineral phase transformations (e.g. Arlt & Angel,
250 2000; Carpenter et al., 2003; Carpenter & Zhang, 2011; McConnell et al., 2000).

251 The linear moduli, k , and their first pressure derivatives, k' , have been obtained by fitting
252 our observed unit-cell parameters at $P_{\text{ruby}} \leq 6.46(2)$ (Supplementary Table S1) with linearized BM3
253 implemented in EosFit7 (Angel et al., 2014). Fit results are listed in Supplementary Table S2. The
254 unit-cell a and b parameters measured at $P_{\text{ruby}} > 6.46(2)$ deviate from the BM3 fit, whereas the c -
255 axis does not exhibit any anomalous behavior in the investigated pressure range (Figure 2b).

256 The axial compressibility of the $P2_1nm$ phase follows the scheme $\beta_b > \beta_a > \beta_c$ (Figure 2b),
257 in agreement with previous reports (Ohira et al., 2019; Sano-Furukawa et al., 2009). This
258 compressibility scheme is due to the different axial response of the δ - $(Al_{0.97}Fe_{0.03})OOH$ structure
259 to compression, with the **a-b** plane being relatively compressible due to the presence of hydrogen
260 bonds in the asymmetric configuration (Supplementary Figure S1a), whereas chains of edge-
261 sharing octahedra extend along the c -axis giving rise to a stiffer unit to be compressed. With
262 increasing pressure, however, the compressibility of the a -axis (and to smaller extent that of the b -
263 axis) decreases quickly as indicated by their relatively large moduli pressure derivatives, which
264 may be due to the shortening of the $O \cdots O$ distance and a consequent increase of the strengths of
265 the hydrogen bonds, as already suggested by previous studies on δ - $AlOOD$ (Sano-Furukawa et al.,

266 2008). After the transition to the high-symmetry phase, a stiffening of the *a*- and *b*- axes in δ -
267 $(\text{Al}_{0.97}\text{Fe}_{0.03})\text{OOH}$ have been previously observed, with the axial compressibilities evolving into a
268 $\beta_c > \beta_a > \beta_b$ scheme (Satta et al., 2021). Thus, our results confirm that the phase transition in δ -
269 $(\text{Al}_{0.97}\text{Fe}_{0.03})\text{OOH}$ induces a marked stiffening of the **a-b** plane, supporting previous findings
270 (Ohira et al., 2019; Sano-Furukawa et al., 2009).

271

272 **3.3. Single-crystal elasticity**

273 A representative Brillouin spectrum collected for crystal H4765x2 at high pressures is
274 shown in Figure 3a, while measured and calculated acoustic velocities obtained for both platelets
275 at the same pressure are shown in Figure 3b. Full elastic stiffness tensors of δ - $(\text{Al}_{0.97}\text{Fe}_{0.03})\text{OOH}$
276 constrained at nine different pressure points are reported in Supplementary Table S3, and
277 individual elastic stiffness coefficients are plotted against pressure in Figure 4.

278 The $P2_1nm$ is a polar space group (i.e. it is not centrosymmetric). Thus, piezoelectricity
279 may exert an influence on acoustic waves velocities propagating in the $P2_1nm$ phase of δ -
280 $(\text{Al,Fe})\text{OOH}$ along specific directions (Every, 1980; Nye, 1985). Here, possible contributions to
281 the acoustic wave velocities from the piezoelectricity were neglected, as in previous Brillouin
282 spectroscopy experiments on δ - AlOOH (Wang et al., 2022). We find this to be a reasonable
283 assumption given the good agreement between our K_{T0} resulting from X-ray diffraction
284 experiments (hence not sensitive to piezoelectricity), and K_{S0} resulting from c_{ij} determined via
285 inversion of observed acoustic wave velocities in a least square fitting of the Christoffel equation.
286 Note also that for those materials for which the piezoelectric tensor has been determined at room
287 pressure, e.g., quartz (Ohno, 1990) and $\text{Ca}_3\text{TaGa}_3\text{Si}_2\text{O}_{14}$ (Ma et al., 2017), a correction of c_{ij}

288 accounting for piezoelectric contribution is <1%, hence further suggesting that the piezoelectric
289 contribution to acoustic wave velocity can be reasonably neglected in our study.

290 The elastic stiffness tensor obtained at room pressure in this study shows a good agreement
291 with the theoretical predictions reported by Cortona (2017), with the exception of c_{22} which is
292 about 20% higher than that determined in this study (Figure 4). Tsuchiya & Tsuchiya (2009)
293 generally report smaller c_{ij} values than those constrained in this study; c_{11} , for example, is about
294 20% smaller. On the other hand, Pillai et al. (2018) report generally larger c_{ij} values compared to
295 those measured here (up to 30%). Our results are also in good agreement with previous Brillouin
296 spectroscopy measurements performed at room pressure on the $P2_{1nm}$ phase of pure δ -AlOOH
297 (Wang et al., 2022) (Figure 4).

298 We found that the pressure dependence of all c_{ij} determined in this study up to $P_{\text{ruby}} =$
299 6.46(2) GPa can be described by a third-order finite strain expression reported for individual c_{ijkl}
300 by Stixrude & Lithgow-Bertelloni (2005):

$$301 \quad c_{ijkl} = (1 + 2f)^{\frac{5}{2}} \{c_{ijkl,0} + (3K_0c'_{ijkl,0} - 5c_{ijkl,0})f + \quad (4)$$
$$+ \left[6K_0c'_{ijkl,0} - 14c_{ijkl,0} - \frac{3}{2}K_0\delta_{kl}^{ij}(3K'_0 - 16)\right]f^2\}$$

302 with the Eulerian strain $f = \left[\left(\frac{V}{V_0}\right)^{-2/3} - 1\right]/2 = \left[\left(\frac{\rho}{\rho_0}\right)^{2/3} - 1\right]/2$, with $c_{ijkl,0}$ and $c'_{ijkl,0}$ being the
303 elastic stiffness coefficients and their pressure derivative at room pressure expressed in full
304 tensorial notation, respectively and with δ_{kl}^{ij} being -3 for c_{1111} , c_{2222} and c_{3333} and -1 for the other
305 six independent coefficients of the elastic tensor.

306 At high pressures, our results are generally in good agreement with previous theoretical
307 predictions at 5 GPa for the $P2_{1nm}$ phase of δ -AlOOH (Cortona, 2017), except for c_{22} and the off-
308 diagonal c_{ij} . Additionally, our results clearly show an elastic softening at $P_{\text{ruby}} > 6.46(2)$ GPa

309 affecting c_{12} , c_{22} and c_{23} . This observation corroborates the presence of an elastic softening
310 observed by our XRD experiments on the axial and volume compression within the same pressure
311 range (Figure 2). The transition to the high-symmetry phase gives rise to an abrupt step increase
312 ($\sim 50\%$) of c_{12} , c_{22} and c_{23} , while all the other c_{ij} show relatively low sensitivity to the phase
313 transition. In general, theoretical studies suggest that the hydrogen bond symmetrization has a
314 severe influence on the elastic behavior of δ -AlOOH. This has been either expressed by a smooth
315 stiffening of the compressional and off-diagonal c_{ij} (Cortona, 2017; Tsuchiya & Tsuchiya, 2009),
316 or by a more complex behavior that may include softening and/or hardening within a relatively
317 short symmetrization pressure range (11-16 GPa) (Pillai et al., 2018). Conversely, our results
318 clearly show that important modifications in the single-crystal elasticity of δ -(Al_{0.97}Fe_{0.03})OOH
319 occur at much lower pressures than previously predicted, and are associated with the structural
320 phase transformation. Additionally, we observed that shear c_{44} , c_{55} and c_{66} only show a limited
321 sensitivity to the transition, in agreement with previous theoretical studies (Cortona, 2017; Pillai
322 et al., 2018; Tsuchiya & Tsuchiya, 2009). Ultimately, it is possible that elastic softening of c_{12} , c_{22}
323 and c_{23} observed in this study may couple with the softening of the O-H stretching optical modes
324 observed in the $P2_1nm$ phase in previous Raman spectroscopy investigations (Wang et al., 2022).

325

326 **3.4. Landau model**

327 As observed above, a 2-4-6 Landau potential well describes the variation with pressure of
328 the order parameter associated with the $P2_1nm \rightarrow Pnmm$ transition in δ -(Al_{0.97}Fe_{0.03})OOH. The
329 same Landau potential can also be used to describe the evolution of the spontaneous strains
330 associated with a displacive phase transition (Carpenter and Salje, 1998), with the Landau
331 expansion being:

$$G = \frac{1}{2}a(P - P_c)Q^2 + \frac{1}{4}bQ^4 + \frac{1}{6}cQ^6 + \lambda_1e_1Q^2 + \lambda_2e_2Q^2 + \lambda_3e_3Q^2 + \frac{1}{2}\sum_{i,j}c_{ij}^0e_ie_j \quad (5)$$

332

333 We note that Equation 5 is identical to that provided by Carpenter et al. (2003) for the
334 *Pmcn* to *P2₁cn* phase transition occurring in lawsonite, but for pressure replacing temperature
335 dependency. In Equation 5, λ_{1-3} are the coupling coefficients between the components of the
336 spontaneous strains and the order parameter Q , e_{1-3} are the spontaneous strain components, and
337 c_{ij}^0 are the “bare”, i.e. not including the effect of the phase transition, elastic stiffness coefficients.

338 In our analysis, the evolution of c_{ij}^0 in the *P2₁nm* stability field is obtained using self-
339 consistent finite strain equations (Equation 4), following the approach delineated by previous
340 studies (e.g. Buchen et al., 2018; Zhang et al., 2021). The extrapolation of c_{ij}^0 to experimental
341 pressures relies on the room pressure elastic stiffness coefficients and respective pressure
342 derivatives constrained for the *Pnmm* phase of δ -(Al_{0.97},Fe_{0.03})OOH by Satta et al. (2021).
343 Spontaneous strain components are defined as (Carpenter et al. 1998):

$$e_1 = \frac{a_L - a_H}{a_H}; \quad e_2 = \frac{b_L - b_H}{b_H}; \quad e_3 = \frac{c_L - c_H}{c_H} \quad (6)$$

345 Where the unit-cell axial lengths (a_L , b_L and c_L) of the *P2₁nm* phase were determined via
346 XRD in this study, and the values of the *Pnmm* phase (a_H , b_H and c_H) at $P < P_c$ were determined
347 using linearized BM3 and the parameters given in Satta et al. (2021).

348 Ultimately, the coupling coefficients λ_{1-3} were constrained in a least-square fitting procedure of
349 spontaneous strain expressions obtained from the Landau expansion under equilibrium conditions
350 (Equations 2-4 in Carpenter et al. 2003). We find the Landau model to provide an excellent
351 description of spontaneous strain components as a function of unit-cell volume compression
352 (Supplementary Figure S3).

353 The variation of individual c_{ij} due to a structural phase transition (Carpenter and Salje 1998)
354 can be defined using the relationship (Slonczewski and Thomas 1970):

$$355 \quad c_{ij} = c_{ij}^0 - \sum_{m,n} \frac{\partial^2 G}{\partial e_i \partial Q_m} \left(\frac{\partial^2 G}{\partial Q_m \partial Q_n} \right)^{-1} \frac{\partial^2 G}{\partial e_j \partial Q_n} \quad (7)$$

356 and considering that for the $P2_1nm \rightarrow Pnmm$ transition only one order parameter Q is active. The
357 relationships between c_{ij}^0 and Q are identical to those previously reported for lawsonite (Equations
358 17-25 in Carpenter et al., 2003). Accordingly, the susceptibility, χ , is defined as:

$$359 \quad \chi^{-1} = \frac{\partial^2 G}{\partial Q^2} = a(P - P_c) + \frac{3b}{a} aQ^2 + \frac{5c}{a} aQ^4 + 2\lambda_1 e_1 + 2\lambda_2 e_2 + 2\lambda_3 e_3 \quad (8)$$

360 which can be seen an adaptation to the expression reported by Carpenter et al. (2003). This
361 adaptation was employed to take into account constraints on b/a and c/a , as well as values the
362 coupling coefficients λ_{1-3} . Here, these parameters were determined in a least-square fitting of Q^2
363 to the intensity ratio $I(0\bar{3}0)/I(1\bar{3}0)$, as previously described in Section 3.1, hence making a the
364 only refined parameter in Equation 8 for c_{11} , c_{22} , c_{33} , c_{12} , c_{13} and c_{23} . As for the coupling coefficient
365 λ_{4-6} , these have been determined by fitting measured c_{44} , c_{55} and c_{66} with appropriate expressions
366 derived from Equation 7, and using the order parameter formulation described above (Equation 3).

367 We found the Landau-based predictions on the high-pressure behavior of c_{ij} to be only in
368 partial agreement to those observed experimentally (Figure 4). Specifically, we note an excellent
369 agreement between observations and Landau-based predictions for the shear c_{44} , c_{55} and c_{66}
370 including a hardening prior to the $P2_1nm \rightarrow Pnmm$ transition. Also, there is a good agreement
371 between observed and predicted c_{33} values, with the only difference being the Landau model
372 predicting a subtle softening prior to the onset of the $P2_1nm \rightarrow Pnmm$ transition and in the $P2_1nm$
373 stability field which was, however, not observed experimentally. On the other hand, only a poor
374 agreement is reached for all other c_{ij} , with experiments and theory agreeing solely on the presence

375 of a softening affecting the c_{12} , c_{22} and c_{23} prior to the onset of the $P2_1nm \rightarrow Pnnm$ transition.
376 Ultimately, the Landau-based model also predicts a softening of the c_{11} and c_{13} , hence contrasting
377 with our experimental observations. Such discrepancies between Landau-based model and
378 experimental observations may suggest that the order parameter associated with the displacive
379 processes is not able to entirely describe the structural changes occurring in $\delta\text{-(Al}_{0.97}\text{,Fe}_{0.03}\text{)OOH}$.
380 Therefore, taking into consideration higher order terms of the coupling between order parameter
381 and spontaneous strain, and/or coupling coefficients dependent on pressure, may be necessary to
382 obtain a better match between Landau prediction and experimental observations. At the same time,
383 it is also possible that differences in relaxation times between proton ordering/disordering and
384 displacive order parameter may play a role in the $P2_1nm \rightarrow Pnnm$ phase transition.

385

386 **3.5. Aggregate properties**

387 All our results on the aggregate properties of $\delta\text{-(Al}_{0.97}\text{,Fe}_{0.03}\text{)OOH}$ are provided in
388 Supplementary Table S4. The adiabatic bulk, K_S , and shear, G , moduli determined in this study at
389 room pressure match previous experimental estimates for $\delta\text{-AlOOH}$ (Wang, et al., 2022), and are
390 in good agreement with most previous theoretical results (Cortona, 2017; Tsuchiya & Tsuchiya,
391 2009). The K_S and G values are shown in Figure 5a as function of pressure. Our results show a
392 marked softening of K_S above 6.46(2) prior to the onset of the $P2_1nm \rightarrow Pnnm$ phase transition,
393 followed by a $\sim 30\%$ increase after the transition to the high-symmetry phase is completed. This
394 elastic softening in K_S is linked to the softening of c_{12} , c_{22} and c_{23} observed in our single-crystal
395 elasticity study. On the other hand, G increases smoothly with pressure and no marked stiffening
396 is observed after the phase transition. The Reuss bound of the adiabatic bulk modulus (K_S^R , Table
397 1) and its pressure derivative are in good agreement with our XRD results. Our results confirm

398 that Al-Fe³⁺ substitution may decrease both K_S and G since values reported for ϵ -FeOOH are
399 sensibly smaller [$K_S = 133(7)$ GPa and $G = 71(2)$ GPa, Ikeda et al., 2019].

400 The calculated aggregate compressional, $v_P (= \sqrt{\frac{K_S^H + 4/3G^H}{\rho}})$ and shear, $v_S (= \sqrt{\frac{G^H}{\rho}})$, wave
401 velocities are listed in Supplementary Table 4. The room pressure v_P and v_S values constrained in
402 this study are in perfect agreement with previous Brillouin spectroscopy results on δ -AlOOH
403 single-crystal elasticity (Wang et al., 2022). At the same time, v_P and v_S determined in this study
404 are respectively about 4% and 7% higher than those observed in polycrystalline δ -AlOOH
405 (Mashino et al., 2016), and about 4% and 10% than those on polycrystalline δ -(Al_{0.95}Fe_{0.05})OOH
406 (Su et al., 2020). These discrepancies between single-crystal and polycrystalline data cannot be
407 ascribed to different Fe content, as Fe substituting Al decreases acoustic wave velocities (Ikeda et
408 al., 2019), but may be related to the presence of lattice preferred orientation in the polycrystalline
409 samples, selective elasto-optic coupling along specific directions (Speziale et al., 2014), the
410 contribution of grain boundaries (Marquardt et al., 2011), or grain-grain-interactions (Wang et al.,
411 2023). The pressure dependencies of both aggregate wave velocities are shown in Figure 5b. As
412 v_P is proportional to the bulk modulus, it is possible to observe a slight softening above 6.46(2)
413 GPa and a jump after the $P2_1nm$ to $Pnmm$ phase transition, whereas v_S show a smooth increase
414 with pressure.

415 **4. Implications**

416 In this study, we provided accurate experimental constraints on the high-pressure, single-
417 crystal elasticity of the $P2_1nm$ phase of δ -(Al_{0.97}Fe_{0.03})OOH and characterised the $P2_1nm \rightarrow Pnmm$
418 phase transition occurring between P_{ruby} 7.59(3) GPa and 7.94(2) GPa. A 2-4-6 Landau potential

419 has been used to describe the variation with pressure of the $I(0\bar{3}0)/I(1\bar{3}0)$ ratio constraining the
420 transition pressure to be $P_c = 7.7(2)$ GPa.

421 Both XRD and Brillouin scattering results show elastic softening occurring in the $P2_1nm$
422 phase prior to the onset of the structural transition. The compressibility of the b - and a -axes
423 increase from 6.46(2) GPa, up to the transition to the $Pnmm$ phase, and is accompanied by a marked
424 softening of the elastic stiffness coefficients c_{12} , c_{22} and c_{23} . These experimental findings were
425 compared to those predicted by a 2-4-6 Landau model which show that the transition has a
426 substantial displacive component with the order parameter and the spontaneous strain having a
427 relaxation time on the order of that probed by the X-ray measurements. However, the Landau
428 model does not reproduce the high-pressure evolution of most of the c_{ij} affected by transition,
429 suggesting that proton order/disorder contributions to the transition may need to be taken into
430 account to describe the elastic behavior of the $P2_1nm$ δ -(Al_{0.97},Fe_{0.03})OOH.

431 The incorporation of the FeOOH component in δ -(Al,Fe)OOH shifts the structural
432 transition toward transition zone pressures (Thompson et al., 2020). If the boundary between the
433 $P2_1nm$ and $Pnmm$ phases is defined by a positive Clapeyron slope, the structural transition and the
434 elastic softening of δ -(Al,Fe)OOH might be occurring in the uppermost Earth's lower mantle
435 (depth >660 km). The relevance of these phenomena in terms of seismic detectability will depend
436 mostly on the volume fraction of δ -(Al,Fe)OOH in subducted lithologies.

437 Ultimately, and in a broader perspective, our results on δ -(Al,Fe)OOH also provide a better
438 understanding of the relation between elasticity and hydrogen dynamics in other O-H \cdots O-bearing
439 materials, such as H₂O ices (e.g. Meier et al., 2018; Shi et al., 2021; Trybel et al., 2020) and phase
440 D (Criniti et al., 2023; Thompson et al., 2022; Tsuchiya et al., 2005), where hydrogen bond
441 symmetrization is predicted as well, although at higher pressures.

442

5. Acknowledgments

443

The authors thank Sumith Abeykoon for helping with the electron microprobe, and Raphael Njul for polishing the crystal platelets. Florian Trybel is acknowledged for fruitful discussions on hydrogen bond symmetrization. Michael Carpenter and another anonymous reviewer are acknowledged for their valuable suggestions. This research was supported by the International Research Training Group “Deep Earth Volatile Cycles” (GRK 2156/1) and the European Union’s Horizon 2020 research and innovation Programme (ERC grant 864877). T. Ishii was supported by the Kakenhi Grant Number JP23K19067. An early draft of this manuscript was included in Satta (2021).

451

6. References

452

Angel, R. J. (2003). Automated profile analysis for single-crystal diffraction data. *Journal of Applied*

453

Crystallography, 36(2), Article 2. <https://doi.org/10.1107/S0021889803001134>

454

Angel, R. J., Alvaro, M., & Gonzalez-Platas, J. (2014). EosFit7c and a Fortran module (library) for equation of state

455

calculations. *Zeitschrift Für Kristallographie - Crystalline Materials*, 229(5). <https://doi.org/10.1515/zkri->

456

2013-1711

457

Angel, R. J., & Finger, L. W. (2011). SINGLE: A program to control single-crystal diffractometers. *Journal of*

458

Applied Crystallography, 44(1), 247–251. <https://doi.org/10.1107/S0021889810042305>

459

Arlt, T., & Angel, R. J. (2000). Displacive phase transitions in C-centred clinopyroxenes: Spodumene, LiScSi₂O₆

460

and ZnSiO₃. *Physics and Chemistry of Minerals*, 27(10), 719–731. <https://doi.org/10.1007/s002690000116>

461

Bercovici, D., & Karato, S. (2003). Whole-mantle convection and the transition-zone water filter. *Nature*,

462

425(6953), 39–44.

463

Boehler, R., & De Hantsetters, K. (2004). New anvil designs in diamond-cells. *High Pressure Research*, 24(3), 391–

464

396. <https://doi.org/10.1080/08957950412331323924>

- 465 Boffa Ballaran, T., Angel, R. J., & Carpenter, M. A. (2000). High-pressure transformation behaviour of the
466 cummingtonite-grunerite solid solution. *European Journal of Mineralogy*, 12(6), 1195–1213.
467 <https://doi.org/10.1127/0935-1221/2000/0012-1195>
- 468 Bolotina, N. B., Molchanov, V. N., Dyuzheva, T. I., Lityagina, L. M., & Bendeliani, N. A. (2008). Single-crystal
469 structures of high-pressure phases FeOOH, FeOOD, and GaOOH. *Crystallography Reports*, 53(6), 960–
470 965. <https://doi.org/10.1134/S1063774508060084>
- 471 Buchen, J. (2018). *The Elastic Properties of Wadsleyite and Stishovite at High Pressures: Tracing Deep Earth*
472 *Material Cycles*. University of Bayreuth. https://doi.org/10.15495/EPub_UBT_00004410
- 473 Buchen, J., Marquardt, H., Schulze, K., Speziale, S., Boffa Ballaran, T., Nishiyama, N., & Hanfland, M. (2018).
474 Equation of State of Polycrystalline Stishovite Across the Tetragonal-Orthorhombic Phase Transition.
475 *Journal of Geophysical Research: Solid Earth*, 123(9), 7347–7360. <https://doi.org/10.1029/2018JB015835>
- 476 Buchen, J., Sturhahn, W., Ishii, T., & Jackson, J. M. (2021). Vibrational anisotropy of δ -(Al,Fe)OOH single crystals
477 as probed by nuclear resonant inelastic X-ray scattering. *European Journal of Mineralogy*, 33(4), 485–502.
478 <https://doi.org/10.5194/ejm-33-485-2021>
- 479 Carpenter, M. A., Angel, R. J., & Finger, L. W. (1990). Calibration of Al/Si order variations in anorthite.
480 *Contributions to Mineralogy and Petrology*, 104(4), 471–480. <https://doi.org/10.1007/BF01575624>
- 481 Carpenter, M. A., Boffa Ballaran, T., & Atkinson, A. J. (1999). Microscopic strain, local structural heterogeneity
482 and the energetics of silicate solid solutions. *Phase Transitions*, 69(1), 95–109.
483 <https://doi.org/10.1080/01411599908208011>
- 484 Carpenter, M. A., McKnight, R. E. A., Howard, C. J., Zhou, Q., Kennedy, B. J., & Knight, K. S. (2009).
485 Characteristic length scale for strain fields around impurity cations in perovskites. *Physical Review B*,
486 80(21), 214101. <https://doi.org/10.1103/PhysRevB.80.214101>
- 487 Carpenter, M. A., Meyer, H.-W., Sondergeld, P., Marion, S., & Knight, K. S. (2003). Spontaneous strain variations
488 through the low temperature phase transitions of deuterated lawsonite. *American Mineralogist*, 88(4), 534–
489 546. <https://doi.org/10.2138/am-2003-0407>
- 490 Carpenter, M. A., Salje, E. K. H., & Graeme-Barber, A. (1998). Spontaneous strain as a determinant of
491 thermodynamic properties for phase transitions in minerals. *European Journal of Mineralogy*, 10(4), 621–
492 691. <https://doi.org/10.1127/ejm/10/4/0621>

- 493 Carpenter, M. A., & Zhang, Z. (2011). Anelasticity maps for acoustic dissipation associated with phase transitions in
494 minerals. *Geophysical Journal International*, 186(1), 279–295. <https://doi.org/10.1111/j.1365->
495 246X.2011.05028.x
- 496 Cortona, P. (2017). Hydrogen bond symmetrization and elastic constants under pressure of δ -AlOOH. *Journal of*
497 *Physics: Condensed Matter*, 29(32), 325505. <https://doi.org/10.1088/1361-648X/aa791f>
- 498 Criniti, G., Ishii, T., Kurnosov, A., Glazyrin, K., Husband, R. J., & Ballaran, T. B. (2023). Structure and
499 compressibility of Fe-bearing Al-phase D. *American Mineralogist*, 108(9), 1764–1772.
500 <https://doi.org/10.2138/am-2022-8559>
- 501 Dewaele, A., Loubeyre, P., & Mezouar, M. (2004). Equations of state of six metals above 94 GPa. *Physical Review*
502 *B*, 70(9), 094112. <https://doi.org/10.1103/PhysRevB.70.094112>
- 503 Every, A. G. (1980). General closed-form expressions for acoustic waves in elastically anisotropic solids. *Physical*
504 *Review B*, 22(4), 1746–1760. <https://doi.org/10.1103/PhysRevB.22.1746>
- 505 Gleason, A. E., Quiroga, C. E., Suzuki, A., Pentcheva, R., & Mao, W. L. (2013). Symmetrization driven spin
506 transition in ϵ -FeOOH at high pressure. *Earth and Planetary Science Letters*, 379, 49–55.
507 <https://doi.org/10.1016/j.epsl.2013.08.012>
- 508 Haussühl, S. (2007). *Physical Properties of Crystals: An Introduction*. Wiley-VCH.
- 509 Hayward, S. A., & Salje, E. K. H. (1996). Displacive phase transition in anorthoclase; the “plateau effect” and the
510 effect of T1-T2 ordering on the transition temperature. *American Mineralogist*, 81(11–12), 1332–1336.
511 <https://doi.org/10.2138/am-1996-11-1204>
- 512 Ikeda, O., Sakamaki, T., Ohashi, T., Goto, M., Higo, Y., & Suzuki, A. (2019). Sound velocity measurements of ϵ -
513 FeOOH up to 24 GPa. *Journal of Mineralogical and Petrological Sciences*, 114(3), 155–160.
514 <https://doi.org/10.2465/jmps.181115b>
- 515 Insiengmay, L., & Stixrude, L. (2023). Hydrogen bond symmetrization and high-spin to low-spin transition of ϵ -
516 FeOOH at the pressure of Earth’s lower mantle. *American Mineralogist*, 108(12), 2209–2218.
517 <https://doi.org/10.2138/am-2022-8839>
- 518 Ishii, T., Criniti, G., Ohtani, E., Purevjav, N., Fei, H., Katsura, T., & Mao, H. (2022). Superhydrous aluminous silica
519 phases as major water hosts in high-temperature lower mantle. *Proceedings of the National Academy of*
520 *Sciences*, 119(44), e2211243119. <https://doi.org/10.1073/pnas.2211243119>

- 521 Jacobsen, S. D. (2006). Effect of Water on the Equation of State of Nominally Anhydrous Minerals. *Reviews in*
522 *Mineralogy and Geochemistry*, 62(1), 321–342. <https://doi.org/10.2138/rmg.2006.62.14>
- 523 Kantor, I., Prakapenka, V., Kantor, A., Dera, P., Kurnosov, A., Sinogeikin, S., Dubrovinskaia, N., & Dubrovinsky,
524 L. (2012). BX90: A new diamond anvil cell design for X-ray diffraction and optical measurements. *Review*
525 *of Scientific Instruments*, 83(12), 125102. <https://doi.org/10.1063/1.4768541>
- 526 King, H. E., & Finger, L. W. (1979). Diffracted beam crystal centering and its application to high-pressure
527 crystallography. *Journal of Applied Crystallography*, 12(4), 374–378.
528 <https://doi.org/10.1107/S0021889879012723>
- 529 Klotz, S., Chervin, J.-C., Munsch, P., & Marchand, G. L. (2009). Hydrostatic limits of 11 pressure transmitting
530 media. *Journal of Physics D: Applied Physics*, 42(7), 075413. [https://doi.org/10.1088/0022-](https://doi.org/10.1088/0022-3727/42/7/075413)
531 [3727/42/7/075413](https://doi.org/10.1088/0022-3727/42/7/075413)
- 532 Komatsu, K., Kuribayashi, T., Sano, A., Ohtani, E., & Kudoh, Y. (2006). Redetermination of the high-pressure
533 modification of AlOOH from single-crystal synchrotron data. *Acta Crystallographica Section E: Structure*
534 *Reports Online*, 62(11), Article 11. <https://doi.org/10.1107/S160053680603916X>
- 535 Kuribayashi, T., Sano-Furukawa, A., & Nagase, T. (2014). Observation of pressure-induced phase transition of δ -
536 AlOOH by using single-crystal synchrotron X-ray diffraction method. *Physics and Chemistry of Minerals*,
537 *41*(4), 303–312. <https://doi.org/10.1007/s00269-013-0649-6>
- 538 Kurnosov, A., Kantor, I., Boffa-Ballaran, T., Lindhardt, S., Dubrovinsky, L., Kuznetsov, A., & Zehnder, B. H.
539 (2008). A novel gas-loading system for mechanically closing of various types of diamond anvil cells.
540 *Review of Scientific Instruments*, 79(4), 045110. <https://doi.org/10.1063/1.2902506>
- 541 Lin, L., Morrone, J. A., & Car, R. (2011). Correlated Tunneling in Hydrogen Bonds. *Journal of Statistical Physics*,
542 *145*(2), 365–384. <https://doi.org/10.1007/s10955-011-0320-x>
- 543 Lindsay, S. M., Anderson, M. W., & Sandercock, J. R. (1981). Construction and alignment of a high performance
544 multipass vernier tandem Fabry–Perot interferometer. *Review of Scientific Instruments*, 52(10), 1478–1486.
545 <https://doi.org/10.1063/1.1136479>
- 546 Luo, C., Umemoto, K., & Wentzcovitch, R. M. (2022). Ab initio investigation of H-bond disordering in
547 δ -AlOOH. *Physical Review Research*, 4(2), 023223.
548 <https://doi.org/10.1103/PhysRevResearch.4.023223>

- 549 Ma, T., Hou, S., Yu, F., Xie, C., Zhang, S., Wang, J., Du, J., Zhan, J., Cheng, X., Wang, S., & Zhao, X. (2017).
550 Electro-elastic characterization of Ca₃TaGa₃Si₂O₁₄ crystals for lateral-field-excitation acoustic wave
551 sensing applications. *Journal of Alloys and Compounds*, 728, 518–524.
552 <https://doi.org/10.1016/j.jallcom.2017.08.284>
- 553 Marquardt, H., Gleason, A., Marquardt, K., Speziale, S., Miyagi, L., Neusser, G., Wenk, H.-R., & Jeanloz, R.
554 (2011). Elastic properties of MgO nanocrystals and grain boundaries at high pressures by Brillouin
555 scattering. *Physical Review B*, 84(6), 064131. <https://doi.org/10.1103/PhysRevB.84.064131>
- 556 Mashino, I., Murakami, M., & Ohtani, E. (2016). Sound velocities of δ-AlOOH up to core-mantle boundary
557 pressures with implications for the seismic anomalies in the deep mantle. *Journal of Geophysical Research: Solid Earth*, 121(2), 595–609. <https://doi.org/10.1002/2015JB012477>
- 559 McConnell, J. D. C., McCammon, C. A., Angel, R. J., & Seifert, F. (2000). The nature of the incommensurate
560 structure in åkermanite, Ca₂MgSi₂O₇, and the character of its transformation from the normal structure.
561 *Zeitschrift Für Kristallographie - Crystalline Materials*, 215(11), 669–677.
562 <https://doi.org/10.1524/zkri.2000.215.11.669>
- 563 Meier, T., Aslandukova, A., Trybel, F., Laniel, D., Ishii, T., Khandarkhaeva, S., Dubrovinskaia, N., & Dubrovinsky,
564 L. (2021). In situ high-pressure nuclear magnetic resonance crystallography in one and two dimensions.
565 *Matter and Radiation at Extremes*, 6(6), 068402. <https://doi.org/10.1063/5.0065879>
- 566 Meier, T., Petitgirard, S., Khandarkhaeva, S., & Dubrovinsky, L. (2018). Observation of nuclear quantum effects
567 and hydrogen bond symmetrisation in high pressure ice. *Nature Communications*, 9(1), Article 1.
568 <https://doi.org/10.1038/s41467-018-05164-x>
- 569 Meier, T., Trybel, F., Khandarkhaeva, S., Laniel, D., Ishii, T., Aslandukova, A., Dubrovinskaia, N., & Dubrovinsky,
570 L. (2022). Structural independence of hydrogen-bond symmetrisation dynamics at extreme pressure
571 conditions. *Nature Communications*, 13(1), 3042. <https://doi.org/10.1038/s41467-022-30662-4>
- 572 Méndez, A. S. J., Trybel, F., Husband, R. J., Steinle-Neumann, G., Liermann, H.-P., & Marquardt, H. (2021). Bulk
573 modulus of H₂O across the ice VII–ice X transition measured by time-resolved x-ray diffraction in
574 dynamic diamond anvil cell experiments. *Physical Review B*, 103(6), 064104.
575 <https://doi.org/10.1103/PhysRevB.103.064104>

- 576 Nishi, M., Tsuchiya, J., Kuwayama, Y., Arimoto, T., Tange, Y., Higo, Y., Hatakeyama, T., & Irifune, T. (2019).
577 Solid Solution and Compression Behavior of Hydroxides in the Lower Mantle. *Journal of Geophysical*
578 *Research: Solid Earth*, 124(10), 10231–10239. <https://doi.org/10.1029/2019JB018146>
- 579 Nye, J. F. (1985). *Physical Properties of Crystals: Their Representation by Tensors and Matrices*. Oxford
580 University Press.
- 581 Ohira, I., Jackson, J. M., Solomatova, N. V., Sturhahn, W., Finkelstein, G. J., Kamada, S., Kawazoe, T., Maeda, F.,
582 Hirao, N., Nakano, S., Toellner, T. S., Suzuki, A., & Ohtani, E. (2019). Compressional behavior and spin
583 state of δ -(Al,Fe)OOH at high pressures. *American Mineralogist*, 104(9), 1273–1284.
584 <https://doi.org/10.2138/am-2019-6913>
- 585 Ohira, I., Ohtani, E., Sakai, T., Miyahara, M., Hirao, N., Ohishi, Y., & Nishijima, M. (2014). Stability of a hydrous
586 δ -phase, AlOOH–MgSiO₂(OH)₂, and a mechanism for water transport into the base of lower mantle. *Earth*
587 *and Planetary Science Letters*, 401, 12–17. <https://doi.org/10.1016/j.epsl.2014.05.059>
- 588 Ohno, I. (1990). Rectangular parallelepiped resonance method for piezoelectric crystals and elastic constants of
589 alpha-quartz. *Physics and Chemistry of Minerals*, 17(5), 371–378. <https://doi.org/10.1007/BF00212204>
- 590 Ohtani, E. (2015). Hydrous minerals and the storage of water in the deep mantle. *Chemical Geology*, 418, 6–15.
591 <https://doi.org/10.1016/j.chemgeo.2015.05.005>
- 592 Ohtani, E. (2020). The role of water in Earth's mantle. *National Science Review*, 7(1), 224–232.
593 <https://doi.org/10.1093/nsr/nwz071>
- 594 Ohtani, E., Litasov, K., Hosoya, T., Kubo, T., & Kondo, T. (2004). Water transport into the deep mantle and
595 formation of a hydrous transition zone. *Physics of the Earth and Planetary Interiors*, 143–144, 255–269.
596 <https://doi.org/10.1016/j.pepi.2003.09.015>
- 597 Panero, W. R., & Stixrude, L. P. (2004). Hydrogen incorporation in stishovite at high pressure and symmetric
598 hydrogen bonding in δ -AlOOH. *Earth and Planetary Science Letters*, 221(1), 421–431.
599 [https://doi.org/10.1016/S0012-821X\(04\)00100-1](https://doi.org/10.1016/S0012-821X(04)00100-1)
- 600 Pernet, M., Joubert, J. C., & Berthet-Colominas, C. (1975). Etude par diffraction neutronique de la forme haute
601 pression de FeOOH. *Solid State Communications*, 17(12), 1505–1510. <https://doi.org/10.1016/0038->
602 [1098\(75\)90983-7](https://doi.org/10.1016/0038-1098(75)90983-7)

- 603 Pillai, S. B., Jha, P. K., Padmalal, A., Maurya, D. M., & Chamyal, L. S. (2018). First principles study of hydrogen
604 bond symmetrization in δ -AlOOH. *Journal of Applied Physics*, 123(11), 115901.
605 <https://doi.org/10.1063/1.5019586>
- 606 Sandercock, J. R. (1982). *Trends in brillouin scattering: Studies of opaque materials, supported films, and central*
607 *modes* (pp. 173–206). Springer, Berlin, Heidelberg. https://doi.org/10.1007/3540115137_6
- 608 Sano-Furukawa, A., Hattori, T., Komatsu, K., Kagi, H., Nagai, T., Molaison, J. J., dos Santos, A. M., & Tulk, C. A.
609 (2018). Direct observation of symmetrization of hydrogen bond in δ -AlOOH under mantle conditions using
610 neutron diffraction. *Scientific Reports*, 8(1), Article 1. <https://doi.org/10.1038/s41598-018-33598-2>
- 611 Sano-Furukawa, A., Kagi, H., Nagai, T., Nakano, S., Fukura, S., Ushijima, D., Iizuka, R., Ohtani, E., & Yagi, T.
612 (2009). Change in compressibility of δ -AlOOH and δ -AlOOD at high pressure: A study of isotope effect
613 and hydrogen-bond symmetrization. *American Mineralogist*, 94(8–9), 1255–1261.
614 <https://doi.org/10.2138/am.2009.3109>
- 615 Satta, N. (2021). *High Pressure Minerals in the Earth and Moon: Understanding the Lunar Impact History and*
616 *Earth's Deep Water Cycle* [Doctoral thesis]. https://doi.org/10.15495/EPub_UBT_00005517
- 617 Satta, N., Criniti, G., Kurnosov, A., Boffa Ballaran, T., Ishii, T., & Marquardt, H. (2021). High-Pressure Elasticity
618 of δ -(Al,Fe)OOH Single Crystals and Seismic Detectability of Hydrous MORB in the Shallow Lower
619 Mantle. *Geophysical Research Letters*, 48(23), e2021GL094185. <https://doi.org/10.1029/2021GL094185>
- 620 Schulze, K., Buchen, J., Marquardt, K., & Marquardt, H. (2017). Multi-sample loading technique for comparative
621 physical property measurements in the diamond-anvil cell. *High Pressure Research*, 37(2), 159–169.
622 <https://doi.org/10.1080/08957959.2017.1299719>
- 623 Shi, W., Sun, N., Li, X., Mao, Z., Liu, J., & Prakapenka, V. B. (2021). Single-Crystal Elasticity of High-Pressure Ice
624 up to 98 GPa by Brillouin Scattering. *Geophysical Research Letters*, 48(8), e2021GL092514.
625 <https://doi.org/10.1029/2021GL092514>
- 626 Simonova, D., Bykova, E., Bykov, M., Kawazoe, T., Simonov, A., Dubrovinskaia, N., & Dubrovinsky, L. (2020).
627 Structural Study of δ -AlOOH Up to 29 GPa. *Minerals*, 10(12), Article 12.
628 <https://doi.org/10.3390/min10121055>
- 629 Speziale, S., Marquardt, H., & Duffy, T. S. (2014). Brillouin Scattering and its Application in Geosciences. *Reviews*
630 *in Mineralogy and Geochemistry*, 78(1), 543–603. <https://doi.org/10.2138/rmg.2014.78.14>

- 631 Stixrude, L., & Lithgow-Bertelloni, C. (2005). Thermodynamics of mantle minerals—I. Physical properties.
632 *Geophysical Journal International*, 162(2), 610–632. <https://doi.org/10.1111/j.1365-246X.2005.02642.x>
- 633 Strozewski, B., Buchen, J., Sturhahn, W., Ishii, T., Ohira, I., Chariton, S., Lavina, B., Zhao, J., Toellner, T. S., &
634 Jackson, J. M. (2023). Equation of State and Spin Crossover of (Al, Fe)-Phase H. *Journal of Geophysical*
635 *Research: Solid Earth*, 128(4), e2022JB026291. <https://doi.org/10.1029/2022JB026291>
- 636 Su, X., Zhao, C., Lv, C., Zhuang, Y., Salke, N., Xu, L., Tang, H., Gou, H., Yu, X., Sun, Q., & Liu, J. (2020). The
637 effect of iron on the sound velocities of δ -AlOOH up to 135 GPa. *Geoscience Frontiers*, 12(2), 937–946.
638 <https://doi.org/10.1016/j.gsf.2020.08.012>
- 639 Sugimura, E., Iitaka, T., Hirose, K., Kawamura, K., Sata, N., & Ohishi, Y. (2008). Compression of H₂O ice to 126
640 GPa and implications for hydrogen-bond symmetrization: Synchrotron x-ray diffraction measurements and
641 density-functional calculations. *Physical Review B*, 77(21), 214103.
642 <https://doi.org/10.1103/PhysRevB.77.214103>
- 643 Suzuki, A. (2010). High-pressure X-ray diffraction study of ϵ -FeOOH. *Physics and Chemistry of Minerals*, 37(3),
644 153–157. <https://doi.org/10.1007/s00269-009-0319-x>
- 645 Suzuki, A., Ohtani, E., & Kamada, T. (2000). A new hydrous phase δ -AlOOH synthesized at 21 GPa and 1000 °C.
646 *Physics and Chemistry of Minerals*, 27(10), 689–693. <https://doi.org/10.1007/s002690000120>
- 647 Thompson, E. C., Campbell, A. J., & Tsuchiya, J. (2017). Elasticity of ϵ -FeOOH: Seismic implications for Earth's
648 lower mantle. *Journal of Geophysical Research: Solid Earth*, 122(7), 5038–5047.
649 <https://doi.org/10.1002/2017JB014168>
- 650 Thompson, E. C., Campbell, A. J., & Tsuchiya, J. (2022). Calculated Elasticity of Al-Bearing Phase D. *Minerals*,
651 12(8), Article 8. <https://doi.org/10.3390/min12080922>
- 652 Thompson, E. C., Davis, A. H., Brauser, N. M., Liu, Z., Prakapenka, V. B., & Campbell, A. J. (2020). Phase
653 transitions in ϵ -FeOOH at high pressure and ambient temperature. *American Mineralogist*, 105(12), 1769–
654 1777. <https://doi.org/10.2138/am-2020-7468>
- 655 Trots, D. M., Kurnosov, A., Boffa Ballaran, T., Tkachev, S., Zhuravlev, K., Prakapenka, V., Berkowski, M., &
656 Frost, D. J. (2013). The Sm:YAG primary fluorescence pressure scale. *Journal of Geophysical Research:*
657 *Solid Earth*, 118(11), 5805–5813. <https://doi.org/10.1002/2013JB010519>

- 658 Trots, D. M., Kurnosov, A., Vasylechko, L., Berkowski, M., Boffa Ballaran, T., & Frost, D. J. (2011). Elasticity and
659 equation of state of Li₂B₄O₇. *Physics and Chemistry of Minerals*, 38(7), 561.
660 <https://doi.org/10.1007/s00269-011-0428-1>
- 661 Trybel, F., Cosacchi, M., Meier, T., Axt, V. M., & Steinle-Neumann, G. (2020). Proton dynamics in high-pressure
662 ice-VII from density functional theory. *Physical Review B*, 102(18), 184310.
663 <https://doi.org/10.1103/PhysRevB.102.184310>
- 664 Trybel, F., Meier, T., Wang, B., & Steinle-Neumann, G. (2021). Absence of proton tunneling during the hydrogen-
665 bond symmetrization in δ -AlOOH. *Physical Review B*, 104(10), 104311.
666 <https://doi.org/10.1103/PhysRevB.104.104311>
- 667 Tsuchiya, J., & Tsuchiya, T. (2009). Elastic properties of δ -AlOOH under pressure: First principles investigation.
668 *Physics of the Earth and Planetary Interiors*, 174(1–4), 122–127.
669 <https://doi.org/10.1016/j.pepi.2009.01.008>
- 670 Tsuchiya, J., Tsuchiya, T., & Tsuneyuki, S. (2005). First-principles study of hydrogen bond symmetrization of phase
671 D under high pressure. *American Mineralogist*, 90(1), 44–49. <https://doi.org/10.2138/am.2005.1628>
- 672 Tsuchiya, J., Tsuchiya, T., Tsuneyuki, S., & Yamanaka, T. (2002). First principles calculation of a high-pressure
673 hydrous phase, δ -AlOOH. *Geophysical Research Letters*, 29(19), 15-1-15–4.
674 <https://doi.org/10.1029/2002GL015417>
- 675 Tsuchiya, T., Tsuchiya, J., Dekura, H., & Ritterbex, S. (2020). Ab Initio Study on the Lower Mantle Minerals.
676 *Annual Review of Earth and Planetary Sciences*, 48(1), 99–119. <https://doi.org/10.1146/annurev-earth-071719-055139>
- 678 Wang, B., Buchen, J., Méndez, A. S. J., Kurnosov, A., Criniti, G., Liermann, H.-P., & Marquardt, H. (2023). Strong
679 Effect of Stress on the Seismic Signature of the Post-Stishovite Phase Transition in the Earth's Lower
680 Mantle. *Geophysical Research Letters*, 50(10), e2023GL102740. <https://doi.org/10.1029/2023GL102740>
- 681 Wang, B., Tan, D., Xiao, W., Ding, X., Li, L., & Song, M. (2022). Raman scattering and Cr³⁺ luminescence study
682 on the structural behavior of δ -AlOOH at high pressures. *American Mineralogist*, 107(10), 1858–1867.
683 <https://doi.org/10.2138/am-2022-8005>

- 684 Wang, B., Zhang, Y., Fu, S., Yan, W., Takahashi, E., Li, L., Lin, J.-F., & Song, M. (2022). Single-crystal elasticity
685 of phase Egg AlSiO₃OH and δ-AlOOH by Brillouin spectroscopy. *American Mineralogist*, 107(1), 147–
686 152. <https://doi.org/10.2138/am-2022-8056>
- 687 Whitfield, C. H., Brody, E. M., & Bassett, W. A. (1976). Elastic moduli of NaCl by Brillouin scattering at high
688 pressure in a diamond anvil cell. *Review of Scientific Instruments*, 47(8), 942–947.
689 <https://doi.org/10.1063/1.1134778>
- 690 Xu, W., Greenberg, E., Rozenberg, G. Kh., Pasternak, M. P., Bykova, E., Boffa-Ballaran, T., Dubrovinsky, L.,
691 Prakapenka, V., Hanfland, M., Vekilova, O. Yu., Simak, S. I., & Abrikosov, I. A. (2013). Pressure-Induced
692 Hydrogen Bond Symmetrization in Iron Oxyhydroxide. *Physical Review Letters*, 111(17), 175501.
693 <https://doi.org/10.1103/PhysRevLett.111.175501>
- 694 Zhang, Y., Fu, S., Wang, B., & Lin, J.-F. (2021). Elasticity of a Pseudoproper Ferroelastic Transition from
695 Stishovite to Post-Stishovite at High Pressure. *Physical Review Letters*, 126(2), 025701.
696 <https://doi.org/10.1103/PhysRevLett.126.025701>
- 697
- 698

699

7. List of Figure Captions

700

701

702

703

704

705

Figure 1. Intensity (I) of the $0\bar{3}0$ reflection normalized with respect to the intensity of the $1\bar{3}0$ reflection collected at the same pressure, and as function of pressure (P). Note that $0\bar{3}0$ is present in the $P2_1nm$ space group and is a systematic absence in the $Pnmm$ space group. Solid line results from a fit to the observed intensity ratios using Equation 3. The inset shows rocking curves (omega scans) of the $0\bar{3}0$ diffraction peak collected at different pressures. Color scale links each curve to its respective collection pressure (values in GPa).

706

707

708

709

710

711

712

713

714

715

716

717

718

Figure 2. a) Unit-cell volume (V/V_0) and b) axial (l/l_0) compression for δ -($\text{Al}_{0.97}\text{Fe}_{0.03}$)OOH as function of pressure (P). Note that the unit-cell volumes and unit-cell axes were normalized with respect their values observed at room pressure. In our data, open symbols represent data points collected in the proximity of the $P2_1nm$ - $Pnmm$ transition, and at pressures of 7.06(5), 7.44(2) and 7.59(3) GPa. These data points were not included in the refinement of BM3 parameters. Solid and dashed lines represent a BM3 fit to our observations (excluding those at $P_{\text{ruby}} \geq 7.06(5)$ GPa) and extrapolations to higher pressures, respectively. Inset in (a) shows differences between pressures determined using the ruby fluorescence P_{ruby} (Table S1 in Supporting Information), and those calculated using the BM3 parameters (P_{calc} , Table S1 in Supporting Information) as a function of P_{ruby} . Error bars are the sum of the uncertainty on P_{ruby} , calculated as the semi-difference between P_{ruby} before and after the XRD measurements, and P_{calc} , obtained by propagating the uncertainties on the BM3 fit parameters using the full covariance matrix.

719

720

721

Figure 3. Results from high-pressure Brillouin spectroscopy experiments on δ -($\text{Al}_{0.97}\text{Fe}_{0.03}$)OOH. a) Representative Brillouin spectrum, collected on H4765x1 at rotation angle (χ) = -30° and $P_{\text{ruby}}=3.85(7)$ GPa. Spectral contributions are assigned to the sample compressional

722 (v_p), fast shear (v_{s1}) and slow shear (v_{s2}) wave velocities, compressional wave velocity of the
723 pressure transmitting medium (Ne) and its backscattered signal (BS), diamond-anvil shear wave
724 velocity (D) and elastic scattering (R). b) Observed (solid symbols) and calculated (solid lines)
725 acoustic wave velocities of both platelets as a function of the rotation angle (χ) at $P_{\text{ruby}}=6.46(2)$
726 GPa.

727 **Figure 4.** Single-crystal elastic stiffness coefficients (c_{ij}) of $\delta\text{-(Al}_{0.97}\text{Fe}_{0.03}\text{)OOH}$ as
728 function of pressure (P). a) c_{11} , c_{22} and c_{33} ; b) c_{44} , c_{55} and c_{66} ; c) c_{12} , c_{13} and c_{23} . Solid and open
729 circles are c_{ij} constrained in this study for the $P2_1nm$ phase of $\delta\text{-(Al}_{0.97}\text{Fe}_{0.03}\text{)OOH}$, while solid
730 squares are c_{ij} of $Pnmm$ phase. Solid line are least square fits to our $P2_1nm$ phase data of third-order
731 finite strain equations (Stixrude & Lithgow-Bertelloni, 2005). Note that c_{ij} constrained at pressures
732 close to the $P2_1nm$ - $Pnmm$ transition [open circles, $P_{\text{ruby}} \geq 7.06(5)$ GPa] were not considered in the
733 fit. Dashed lines are extrapolation of the $P2_1nm$ phase data fit. Dash-dot lines show the high-
734 pressure behaviour of c_{ij} belonging to the $Pnmm$ phase of $\delta\text{-(Al}_{0.97}\text{Fe}_{0.03}\text{)OOH}$ as reported by Satta
735 et al. (2021). The short-dotted lines show the Landau-based model predictions for c_{ij} in the $P2_1nm$
736 phase field. Solid vertical line shows transition pressure [$P_c = 7.7(2)$ GPa] as determined from fit
737 of Q^2 to experimental observations, with the grey region indicating the uncertainty on the transition
738 pressure. Literature references for $\delta\text{-AlOOH}$ are: 1) Wang et al. (2022); 2) Cortona (2017); 3)
739 Tsuchiya & Tsuchiya (2009); 4) Pillai et al. (2018).

740 **Figure 5.** Aggregate properties of $\delta\text{-(Al}_{0.97}\text{Fe}_{0.03}\text{)OOH}$ as function of pressure (P): a)
741 aggregate elastic modulus (M); b) aggregate velocity (v). For this study, solid and open circles are
742 values calculated for the $P2_1nm$ phase of $\delta\text{-(Al}_{0.97}\text{Fe}_{0.03}\text{)OOH}$, while solid squares are those of the
743 $Pnmm$ phase. Solid line results from least square fits to our $P2_1nm$ phase data of third-order finite
744 strain equations (Stixrude & Lithgow-Bertelloni, 2005). Note that the values constrained at

745 pressures close to the $P2_1nm \rightarrow Pnnm$ transition (open circles, $P_{\text{ruby}} \geq 7.06(5)$ GPa) were not
746 considered in the fit. Dashed lines are extrapolation of the $P2_1nm$ phase data fit. Dashed-point lines
747 show the high-pressure behaviour of c_{ij} of the $Pnnm$ phase of $\delta\text{-(Al}_{0.97}\text{,Fe}_{0.03}\text{)OOH}$ from Satta et
748 al. (2021). The short-dotted lines show the Landau-based model predictions for c_{ij} in the $P2_1nm$
749 phase field. Solid vertical line shows transition pressure [$P_c = 7.7(2)$ GPa] as determined from fit
750 of Q^2 to experimental observations, with the grey region indicating the uncertainty on the transition
751 pressure. In Figure a), literature references for $\delta\text{-AlOOH}$ are: 1) Wang et al. (2022); 2) Cortona
752 (2017); 3) Tsuchiya & Tsuchiya (2009); 4) Pillai et al. (2018). In Figure b), literature references
753 are: 1) Wang et al. (2022); $\delta\text{-AlOOH}$; 2) Mashino et al. (2016), $\delta\text{-AlOOH}$; 3) Su et al. (2020), $\delta\text{-}$
754 $(\text{Al}_{0.95}\text{,Fe}_{0.05}\text{)OOH}$
755

756

757

8. Tables

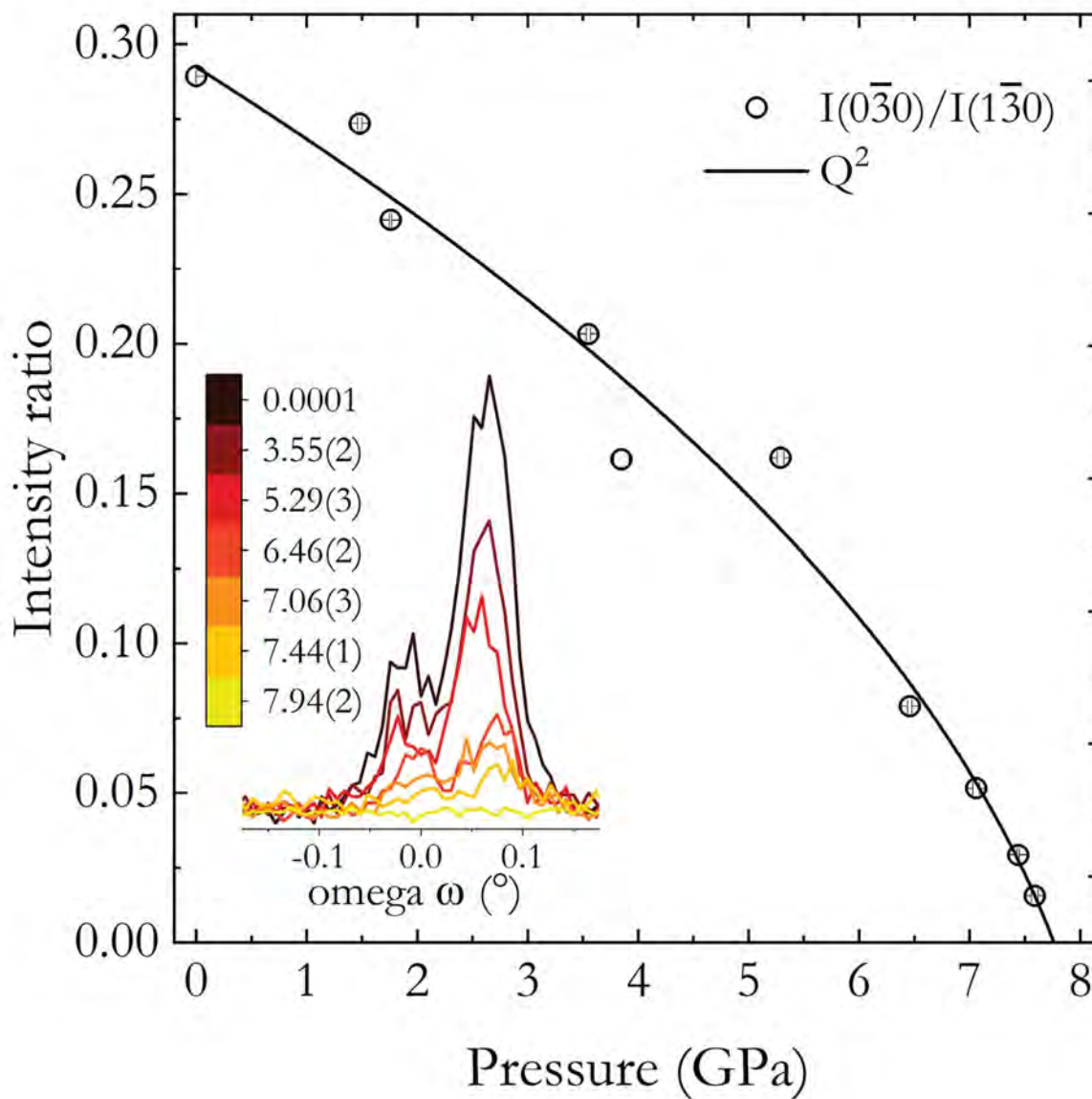
758 **Table 1.** Elastic stiffness coefficients (c_{ij}), aggregate elastic moduli (M_0) and their pressure
 759 derivatives (M'_0) of the $P2_1nm$ phase of $\delta-(Al_{0.97},Fe_{0.03})OOH$. Results are obtained from the fit of
 760 third-order Eulerian strain equations (Equation 4) to c_{ij} constrained at $P_{\text{ruby}} \leq 6.46(5)$ GPa.

ij	c_{ij0} (GPa)	c'_{ij0}		M_0 (GPa)	M'_0
11	370(2.6)	9.9(5)	Voigt Bound		
22	300(4)	5(1)	K_{S0}^V	165(2)	3.6(5)
33	413(4)	5.1(9)	G_0^V	143(1)	2.7(2)
44	127.6(13)	2.6(2)	Reuss Bound		
55	127.4(8)	1.6(2)	K_{S0}^R	160(2.2)	3.6(5)
66	169(2)	4.4(5)	G_0^R	141(1)	2.7(2)
12	48(4)	1.7(10)	Voigt-Reuss-Hill average		
13	98(3)	2.4(7)	K_{S0}^H	163(2)	3.6(5)
23	59(4)	1.6(9)	G_0^H	142(1)	2.7(2)

761

762

763 **9. Figures**



764

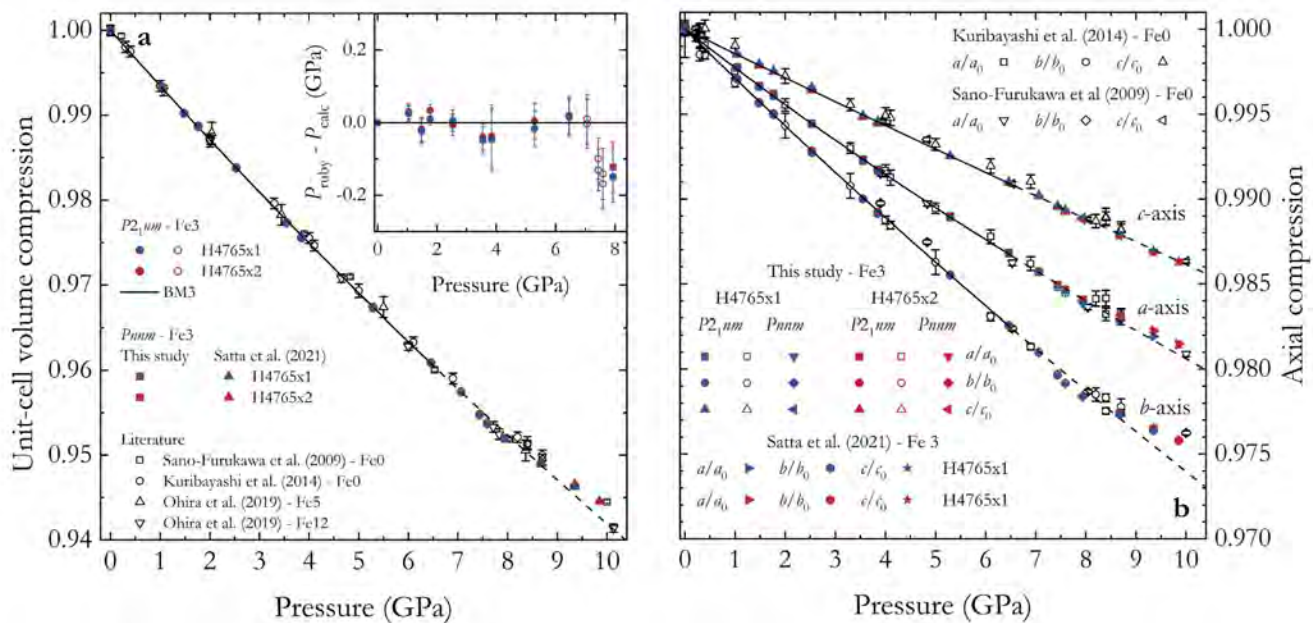
765

Figure 1.

Revised manuscript submitted to: *American Mineralogist*

766

767

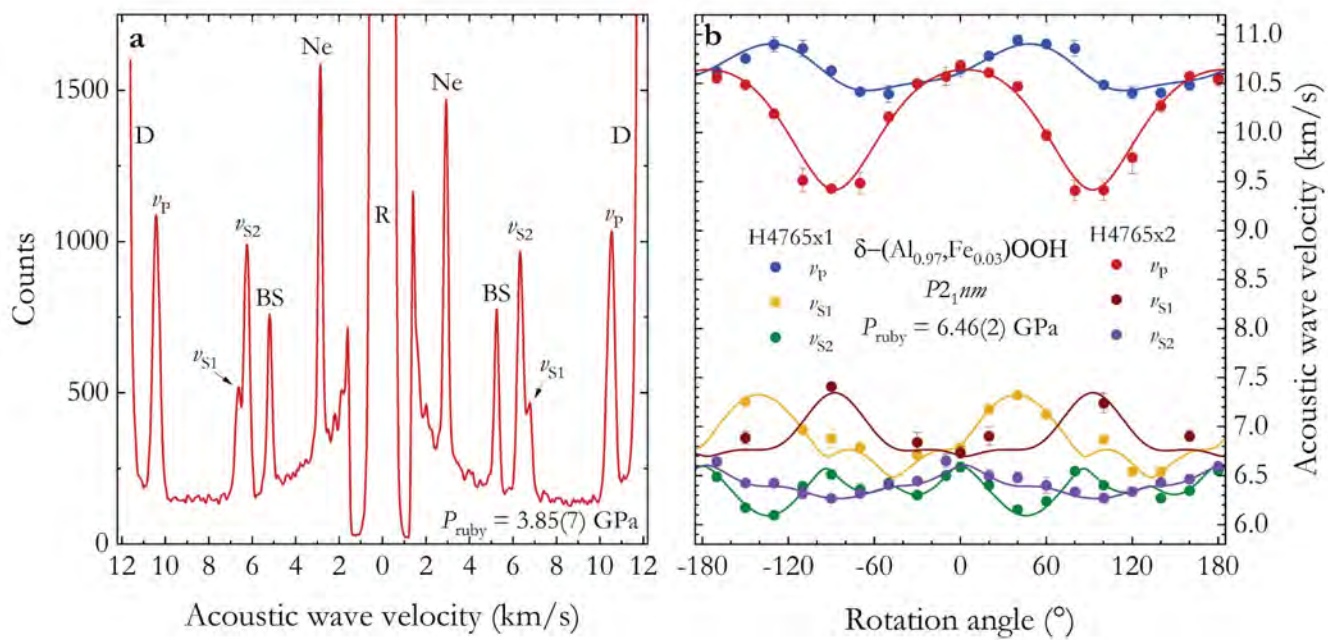


768

769 **Figure 2.**

770

Revised manuscript submitted to: *American Mineralogist*

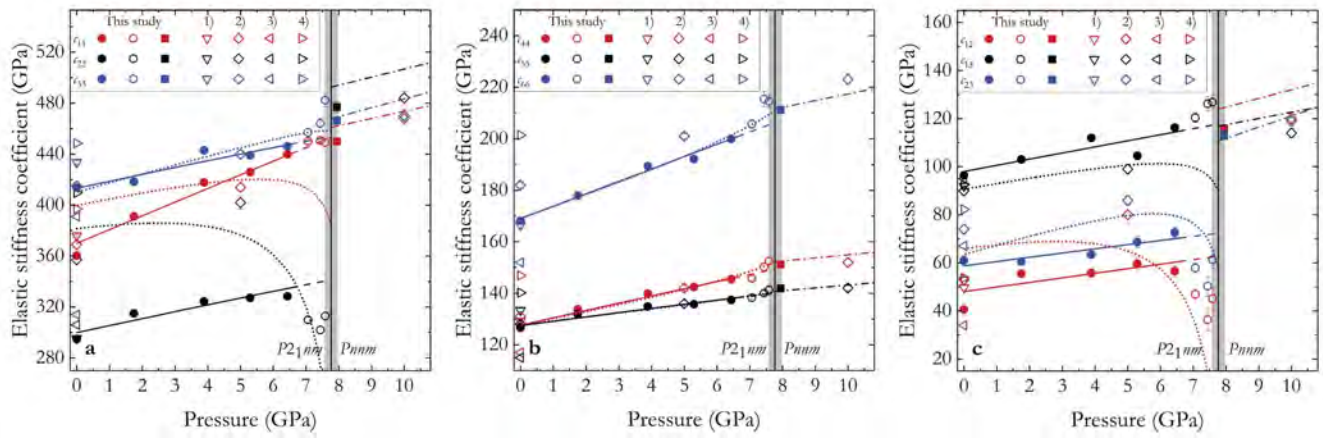


771

772 **Figure 3.**

Revised manuscript submitted to: *American Mineralogist*

773



774

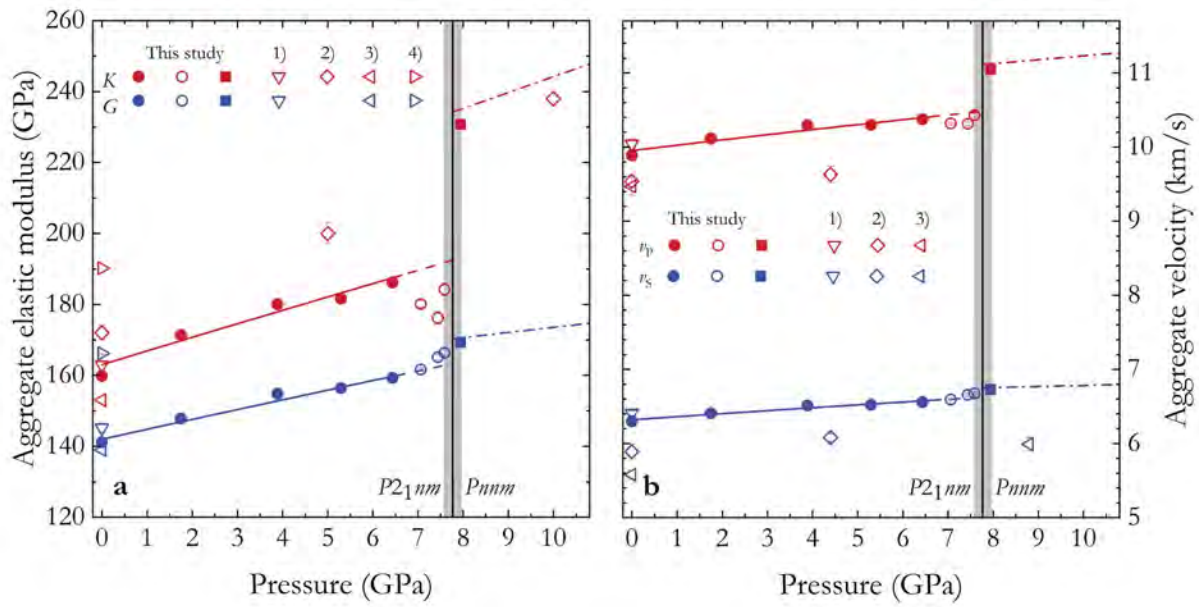
775 **Figure 4.**

776

777

778

Revised manuscript submitted to: *American Mineralogist*



779

780 **Figure 5**